Discrete-dual-porosity model for electric current flow in fractured rock

Delphine Roubinet[1] and James Irving[1]

Corresponding author: D. Roubinet (delphine.roubinet@gmail.com)

[1]Applied and Environmental Geophysics Group, Faculty of Geosciences and Environment, University of Lausanne, Switzerland.

Abstract. The identification of fractures and the characterization of their properties is of critical importance in a wide variety of research fields and applications. To this end, geophysical methods are of significant interest as they can provide information regarding the spatial distribution of a number of subsurface physical properties in a rapid and non-invasive manner. Electrical resistivity surveying, in particular, has been shown in several previous investigations to exhibit sensitivity to the presence of fractures, suggesting that geoelectrical experiments may contain important information regarding how fractures are distributed and connected in the subsurface. However, a lack of suitable numerical modeling tools for electric current flow in fractured media has prevented a detailed and systematic exploration of this concept. To address this issue, we present a novel discrete-dual-porosity modeling approach that is specifically tailored to the electrical resistivity problem. With our approach, an analytical formulation for fracture-matrix current flow exchange at the fracture-scale is integrated into a discrete-fracture-network model, which is then combined with a block-scale finite-volume representation of the rock matrix. Our methodology allows for low-cost and accurate simulation of electric current flow through both the fractures and matrix, and is readily applicable to complex fracture networks at relatively large scales. Although formulated here in two dimensions, this work represents an important first step towards investigating the effect of fracture-network characteristics on bulk electrical properties, as well as towards the simulation of geoelectrical survey data in realistic fractured-rock environments.

1. Introduction

The study of fractured rocks is critically important in a wide variety of research fields and applications including hydrogeology, geothermal energy, hydrocarbon extraction, and the long-term storage of toxic waste (e.g., *Carneiro* [2009]; *Dershowitz and Miller* [1995]; *Gautam and Mohanty* [2004]; *Kolditz and Clauser* [1998]; *Rotter et al.* [2008]). Fractured media are characterized by a large contrast in permeability between the fractures and the surrounding rock matrix, with the highly permeable fractures typically occupying an extremely small volume of the lower permeability host domain. For hydrocarbon extraction, the presence of fractures is a key advantage as they permit quick and easy access to the resource. For toxic waste storage and in contaminated regions, however, fractures represent a significant problem as there is a greatly increased risk of leakage and migration of pollutants deep into the subsurface. In all cases, the identification of fracture, and fracture network, characteristics is a critical and challenging step that is required for future predictions of flow and transport in the subsurface, as well as for the development of appropriate management and decision making strategies.

Given the importance of fractured rocks and their characterization, a vast amount of research has been devoted to how we can most effectively gather information about fractures in the subsurface, i.e., their geometry, their physical properties, and the way in which they are distributed and connected (e.g., *Berkowitz* [2002]; *Bonnet et al.* [2001]; *Neuman* [2005]). Of particular interest has been the use of geophysical methods for fracture and fracture network characterization, as these methods are able to provide information on the distribution of various subsurface physical properties in a rapid and largely non-invasive manner. This is in contrast to more traditional measurement techniques in fractured rock environments, which typically rely upon direct observation of fractures and/or experimentation at a small number of borehole locations throughout the domain of interest, combined with larger-scale observations of flow and transport behavior.

Many, if not most, geophysical methods have been previously investigated to varying degrees in the context of fractured rock. These include seismic, ground-penetrating radar, electrical resistivity, induced polarization, self potential, and electromagnetic methods (e.g., *Day-Lewis* [2003]; *Dorn et al.* [2011, 2012]; *Donadille and Al-Ofi* [2012]; *Herwanger et al.* [2004a]; *Krautblatter et al.* [2010]; *Liu* [2005]; *Lofi et al.* [2012]; *Lubbe and Worthington* [2006]; *Majer et al.* [1997]; *Pytharouli et al.* [2011]; *Queen and Rizer* [1990]; *Robinson et al.* [2013]; *Schmutz et al.* [2011]; *Tsoflias and Hoch* [2006]; *Talley et al.* [2005]; *Wishart et al.* [2008]). Here, we focus on the electrical resistivity method for the reasons that (i) a large body of previous work has indicated that the presence of fractures commonly has a significant influence on field geoelectrical measurements, especially as a function of direction or azimuth, and thus that these measurements may contain important information regarding the fracture distribution (e.g., *Boadu et al.* [2005]; *Busby* [2000]; *Lane et al.* [1995]; *Taylor and Fleming* [1988]); (ii) geoelectrical measurements can be acquired in a straightforward manner along the Earth's surface and/or from boreholes in order to estimate the distribution of subsurface electrical resistivity at a range of spatial scales; and (iii) the presence of fractures in a rock represents preferential pathways for the flow of both water and electric current, which suggests that hydraulically relevant information on fracture network properties may be obtained from geoelectrical data. In particular, we focus in this paper on the numerical modeling of electric current flow in fractured rock, which so far has been constrained by computational limitations to small domains containing relatively few fractures and/or simple configurations that are not representative of realistic field conditions. The development of accurate and efficient modeling tools for electric current flow in realistic fracture networks is an absolutely essential first step towards understanding how fractures affect overall electrical properties and geoelectrical survey measurements, as well as for the eventual development of appropriate inversion strategies.

Existing numerical modeling tools for electric current flow in geological materials are not well adapted to deal with the specific challenges of fractured media, which prevents us from fully exploring the potential of geoelectrical experiments to characterize fracture network properties. In particular, the majority of existing approaches are based upon fully discretized numerical approximations of the Poisson equation, made using either finite-difference, finite-element, or finite-volume techniques (e.g., *Dey and Morrison* [1979]; *Pidlisecky and Knight* [2008]; *Rücker et al.* [2006]), in which one considers explicitly all of the heterogeneities above a certain mesh size and assumes that continuum behavior can be assigned at the sub-mesh scale. While this type of approach may be appropriate for modeling electric current flow in non-fractured porous media, it poses severe problems for fractured rock because of the strong contrast in electrical resistivity that exists between the fractures and matrix and the small spatial dimension of the fractures as compared to the domain size of interest. Consider, for example, a fractured domain at the meter scale where the fracture aperture ranges from the micrometer- to the millimeter-scale, which results in a gap between the smallest and largest characteristic lengths between 3 and 6 orders of magnitude. Even for this simple case, attempting to model the fractures explicitly (i.e., where the mesh size corresponds to the smallest characteristic length) will be extremely computationally expensive, and computational costs for larger fractured domains will be unrealistic, even in the context of two dimensional problems. Although meshing and/or numerical techniques may be adapted to the presence of fractures to allow for a decrease in the computational cost of such a fully discretized solution (e.g., *Berg and Oian* [2007]; *Haegland et al.* [2009]; *Robinson et al.* [2013]), this will generally not result in enough of an improvement for the consideration of realistic fracture networks. One possible solution to this problem is to homogenize the effect of the fractures below some larger mesh scale, thereby reducing the total number of model elements and hence the computational complexity (e.g., *Herwanger et al.* [2004b]). However, in doing this we implicitly assume that the fractured medium can be treated as a representative elementary volume (REV) at that larger scale, having well defined tensor properties, which may not be the case except when dealing with very dense fracture distributions. Another potential means of overcoming computational issues is to use effective-medium-type methods and/or analytical solutions, a variety of which have been developed for the electrical properties of fractured rock (e.g., *Berryman and Hoversten* [2013]; *Campbell* [1977]; *Jinsong et al.* [2009]). However, such methods are restricted to rather simple, idealized fracture networks and are not able to deal with fracture configurations and scales that are commonly encountered in the field.

In the domain of fractured rock hydrology, the lack of existence of an REV for the hydraulic conductivity of realistic fracture configurations has led to the development of a computationally efficient, explicit representation of fracture networks for groundwater flow modeling known as the discrete fracture network (DFN) approach (e.g., *Cacas et al.* [1990];

Dverstop and Andersson [1989]; *Long et al.* [1982]). In this approach, the dimensionality of the problem is greatly reduced by considering flow to occur only through the connected fracture network, as well as by treating the fractures as simplified geometrical elements such as disks, lines, or planes (e.g., *de Dreuzy et al.* [2013]; *Dershowitz and Einstein* [1988]; *Dershowitz and Fidelibus* [1999]; *Pichot et al.* [2012]). In a variety of previous studies, the DFN approach has been demonstrated to be an accurate and efficient method for groundwater flow modeling in many fractured-rock environments (e.g., *Cvetkovic et al.* [2004]; *Davy et al.* [2006]; *Roubinet et al.* [2010a]). Indeed, the restriction of flow to a well connected fracture domain is commonly justified in hydrological investigations where there exists a many-orders-of-magnitude difference between the transmissivity of the fractures and the permeability of the rock matrix. For the modeling of electric current flow in fractured rock, however, direct application of the DFN approach is not appropriate because the contribution of flow through the matrix cannot be ignored. That is, the difference in electrical resistivity between the fractures and the host rock may be around only two orders of magnitude, and thus a non-negligible amount of the total electric current flow will occur through the matrix, as well as through 'dead-end' fractures that are not connected to the main network. Further, as geoelectrical surveying is typically conducted using point electrodes that are not coincident with fracture locations, accounting for current flow through the matrix is necessary even in cases where its electrical conductivity is negligible when compared to the fractures.

In order to combine the low-cost computational advantages of the DFN approach with an explicit representation of the matrix in cases where the host rock permeability cannot be ignored, the concept of discrete-dual-porosity (DDP) modeling has been proposed in hydrology for single and multi-phase subsurface flow modeling [*Lee et al.*, 2001; *Li and Lee*, 2008]. With this approach, flow through the fracture network is modeled using the DFN method, whereas the matrix is discretized on a coarser grid upon which flow can be modeled using standard finite-volume-type approaches. Flow in the fracture and matrix domains is not independent, in the sense that coupling is enforced through a flow-exchange coefficient that is defined at the size of the matrix mesh. Advantages of the DDP approach are that it allows for the consideration of matrix flow and heterogeneous matrix properties when deemed important, as well as for the free choice of source terms within either the fracture network or matrix. However, the approximations for the fracture-matrix flow exchange upon which existing DDP formulations rely are not generally well adapted for the modeling of electric current flow in fractured media because of the lesser contrast in electrical conductivity between fractures and matrix as compared with the hydraulic conductivity. Specifically, existing DDP formulations neglect variability in the potential along fractures within a matrix block, which may result in sizable errors in cases where significant flow exchange occurs between the fractures and the matrix. In order to reduce such errors and reach accurate simulations in the case of electric current flow, the matrix must be discretized more finely; however this comes at an increased computational cost.

In this paper, with the overall goal of finding an optimal balance between computational cost and representation accuracy, we build on the DDP concept described above and present a novel methodology for the modeling of electric current flow in fractured rock. In particular, we present an analytical formulation for fracture-matrix flow exchange at the fracture-scale, developed specifically for the electrical resistivity problem, which is then integrated into a global numerical modeling scheme at the domain-scale. Our modified

DDP approach allows us to take into account the variation in electric potential within the fracture network while maintaining a coarse discretization of the matrix, and has the capacity for dealing with highly heterogeneous and dense fracture distributions at extremely low computational cost when compared to fully discretized solutions. We focus in this paper on modeling electric current flow in all generality, which represents a critical first step for future investigations into the effects of fracture network characteristics on (i) bulk electrical properties, (ii) the existence of an REV for the electrical resistivity, and (iii) geoelectrical survey measurements. While the formulation presented herein is limited to two dimensions for ease of presentation and simplicity, the overall approach should be extendable to three dimensions and permit electric current flow modeling in realistic fractured-rock environments.

We begin by presenting the mathematical development of our proposed approach along with details of its numerical implementation. Next, we validate the approach against analytical and fully-discretized finite-element solutions for three simple fracture networks. Finally, we present two example applications of the modeling methodology, the first being to study the impact of fractures on equivalent electrical resistivity anisotropy, and the second being to study how fractures affect the spatial distribution of electric potential arising from a point current source.

2. Methodology

2.1. Governing equations

Under steady-state conditions, electric current flow is governed by the following charge conservation equation at the point scale:

$$\nabla \cdot \mathbf{J} = Q \quad (1)$$

where $\mathbf{J}$ is the current density (A m^{-2}, A: Amperes) and Q (C m^{-3} s^{-1}, C: Coulombs) is a source (positive) or sink (negative) term corresponding to an electric charge q (C) per unit volume per unit time. Expressing the current density through Ohm's Law as $\mathbf{J} = -\sigma\nabla\phi$, where σ is the electrical conductivity (S m^{-1}, S: Siemens) and ϕ is the electric potential (V, V: Volts), leads to the following equation:

$$-\nabla \cdot (\sigma\nabla\phi) = Q, \quad (2)$$

which forms the basis for all geoelectrical modeling techniques.

2.2. Overall modeling strategy

Modeling electric current flow in fractured media requires us to consider current propagation through both the fracture and matrix domains, as the difference in electrical conductivity between these domains is generally not great enough to consider flow through the fractures only. To this end, our developed DDP approach considers separately charge conservation at the fracture, fracture-network, and matrix scales through equation (2), and accounts for current flow between the fractures and matrix based on the difference in electric potential between them. Formulation of the approach involves the following three steps, which are described in detail in the sections to follow:

1. Derivation of an analytical expression for the electric potential along a fracture segment considering the possibility of fracture-matrix exchange, i.e., current flow from the fracture into the surrounding matrix and *vice versa* (Section 2.4).

2. Development of a system of linear equations describing charge conservation at the fracture-network scale with fracture-matrix exchange. Here, a modified DFN approach is utilized based on the results from Step 1 (Section 2.5).

3. Development of another system of linear equations, which completes the system described in Step 2, describing charge conservation in the matrix with fracture-matrix exchange. Here, a modified finite-volume method is employed based on results from Step 1 (Section 2.6).

2.3. Model discretization and nomenclature

We discretize the matrix in the subsurface domain of interest into regular cells or blocks, which are identified by the indices (I, J), where $I = 1, ..., N_X$ and $J = 1, ..., N_Y$, with N_X and N_Y being the number of blocks in the longitudinal and transverse directions, respectively. Figure 1 illustrates a fractured porous domain where the matrix has been discretized into three blocks in each direction, with the blocks being represented by blue squares containing the corresponding indices (I, J). Fractures in the considered domain are represented by 1D elements that have been subdivided into segments, where the total number of segments required to describe the fractures is determined by the number of nodes. These nodes are comprised of fracture extremities, fracture intersections, and the intersections between fractures and matrix block boundaries. In Figure 1, three fractures are illustrated, which have been subdivided into 10 segments defined by 12 nodes. Nodes 1, 6, 7, 9, 10, and 12 (red circles) correspond to fracture extremities, nodes 2, 4, 5, 8, and

11 (black circles) to intersections between fractures and the matrix block boundaries, and node 3 (green circle) to a fracture intersection. We denote each fracture segment k to be delimited by the nodes i_k and j_k and characterized by aperture b_f^k (m) and electrical conductivity σ_f^k. The electric potential along each fracture segment is denoted by ϕ_f^k, and the potential values at the endpoints by $\varphi_f^{i_k}$ and $\varphi_f^{j_k}$. At the block scale, the matrix electrical conductivity and potential are denoted by $\sigma_m^{I,J}$ and $\phi_m^{I,J}$, respectively (Figure 2). Note that, in the development presented below, lower-case indices (i_k, j_k) will always be used to describe fracture segment nodes and upper-case indices (I, J) to describe matrix block coordinates. We will also commonly refer to a matrix block as a control volume (denoted by $V_{I,J}$), as this is common terminology within the finite-volume community.

2.4. Analytical expression for the electric potential along a fracture segment

Considering a 1D fracture segment k delimited by nodes i_k and j_k and having a constant electrical conductivity σ_f^k along its length, equation (2) leads to the following expression involving the electric potential ϕ_f^k along the segment:

$$-\sigma_f^k \frac{\partial^2 \phi_f^k}{\partial x_k^2} = -Q_{fm} \tag{3}$$

where x_k denotes the spatial variable going from i_k to j_k, and the source term Q_{fm} corresponds to the exchange of electric current between the fracture segment and the surrounding matrix. In the case where electric current travels from the fracture into the matrix, we define Q_{fm} to be positive. Conversely, for current flow from the matrix into the fracture, Q_{fm} will be negative. Note that this definition of Q_{fm}, which is the same in our treatment of the matrix in Section 2.6, necessitates the additional negative sign on the source term in equation (3) as compared to equation (2).

Assuming that the fracture-matrix exchange can be expressed as the product of some exchange coefficient $\alpha_{fm}^{I,J}$, defined at the matrix block scale, and the difference between the fracture and matrix electric potentials [*Carrera et al.*, 1998; *Haggerty and Gorelick*, 1995; *Noetinger et al.*, 2001], i.e., assuming that

$$Q_{fm} = -\alpha_{fm}^{I,J}(\phi_m^{I,J} - \phi_f^k), \tag{4}$$

equation (3) can be rearranged as follows:

$$\frac{\partial^2 \phi_f^k}{\partial x_k^2} - \Gamma_{I,J}^k \phi_f^k = -\Gamma_{I,J}^k \phi_m^{I,J}, \tag{5}$$

where $\Gamma_{I,J}^k \equiv \alpha_{fm}^{I,J}/\sigma_f^k$. Details on an appropriate choice for the block-scale exchange coefficient $\alpha_{fm}^{I,J}$ are provided in Section 2.7.

We now wish to solve equation (5) for the spatially varying electric potential along the fracture segment, $\phi_f^k = \phi_f^k(x_k)$. Defining L_k as the length of the segment, the endpoint nodes i_k and j_k will be located at $x_k = 0$ and $x_k = L_k$, respectively (Figure 2). Considering Dirichlet boundary conditions with electric potentials $\varphi_f^{i_k}$ and $\varphi_f^{j_k}$ at these locations, we arrive at the following:

$$\phi_f^k(x_k) = C_1 \exp\left(\sqrt{\Gamma_{I,J}^k} x_k\right) + C_2 \exp\left(-\sqrt{\Gamma_{I,J}^k} x_k\right) + \phi_m^{I,J}, \tag{6}$$

where constants C_1 and C_2 are given by

$$C_1 = \varphi_f^{i_k} - C_2 - \phi_m^{I,J} \tag{7a}$$

$$C_2 = \frac{\varphi_f^{j_k} - \phi_m^{I,J} - \left(\varphi_f^{i_k} - \phi_m^{I,J}\right) \exp\left(\sqrt{\Gamma_{I,J}^k} L_k\right)}{\gamma(L_k)} \tag{7b}$$

with

$$\gamma(x_k) = \exp\left(-\sqrt{\Gamma_{I,J}^k} x_k\right) - \exp\left(\sqrt{\Gamma_{I,J}^k} x_k\right).$$

Expression (6) can be rewritten as

$$\phi_f^k(x_k) = \beta(x_k)\varphi_f^{i_k} + \frac{\gamma(x_k)}{\gamma(L_k)}\varphi_f^{j_k} + \left[1 - \frac{\gamma(x_k)}{\gamma(L_k)} - \beta(x_k)\right]\phi_m^{I,J} \tag{8}$$

with

$$\beta(x_k) = \exp\left(\sqrt{\Gamma_{I,J}^k}x_k\right) - \frac{\gamma(x_k)}{\gamma(L_k)}\exp\left(\sqrt{\Gamma_{I,J}^k}L_k\right).$$

This expression for the electric potential along a fracture segment can be seen to depend on the potential values at the segment extremities as well as on the potential of the surrounding matrix block. We use this result below to integrate fracture-matrix exchange into a modified DFN formulation for the fracture network, and into a modified finite-volume approach for the matrix domain.

2.5. Modified DFN approach for the fracture network

The DFN modeling approach in fractured-rock hydrology is based upon the principle of mass conservation at each fracture intersection (e.g., *Cacas et al.* [1990]; *Long et al.* [1982]). Considering electric current circulating in a fracture network, we can, in a similar manner, enforce charge conservation at each fracture intersection node i by integrating equation (2) over a small volume V_i containing the intersection. Using Gauss's Divergence Theorem and assuming a lack of sources or sinks at the intersection location, this leads to the following:

$$\int_{S_i} \sigma\nabla\phi \cdot \vec{n}_{S_i}\mathrm{d}S = 0, \tag{9}$$

where S_i is the surface contour of V_i and $\vec{n}_{S_i}$ is its outward unit normal vector. Now considering intersection node i as the shared extremity of N_i fracture segments distinguished by their second node j_k and having aperture b_f^k and electrical conductivity σ_f^k, equation (9) can be approximated as

$$\sum_{k=1}^{N_i} b_f^k \sigma_f^k \frac{\partial \phi_f^k}{\partial x_k}\bigg|_{|x_k=0} = 0. \tag{10}$$

As an example, Figure 3 shows a zoom of the fracture intersection in matrix block $(1, 2)$ from Figure 1, where node 3 is the intersection point. This node is the shared extremity of 4 fracture segments distinguished by their second extremities (nodes 2, 4, 7, and 8) and denoted by $k = 1, 2, 3,$ and 4, respectively. Each fracture segment is characterized by a constant aperture b_f^k and electrical conductivity σ_f^k, with the electric potential $\phi_f^k = \phi_f^k(x_k)$ varying along its length. For this particular configuration, mass conservation at the fracture intersection is given by equation (10) with $N_i = 4$.

In contrast to a standard DFN approach that assumes a linear variation of hydraulic potential between the fracture endpoints, we calculate the derivative in equation (10) using the analytical expression for the electric potential derived earlier and given by equation (6), thus allowing for fracture-matrix current flow exchange. This yields

$$\begin{aligned}\frac{\partial \phi_f^k}{\partial x_k} =& C_1 \sqrt{\Gamma_{I,J}^k} \exp\left(\sqrt{\Gamma_{I,J}^k} x_k\right) \\ & - C_2 \sqrt{\Gamma_{I,J}^k} \exp\left(-\sqrt{\Gamma_{I,J}^k} x_k\right).\end{aligned} \tag{11}$$

Equation can be rewritten as follows:

$$\frac{\partial \phi_f^k}{\partial x_k} = a_{i_k} \varphi_f^{i_k} + a_{j_k} \varphi_f^{j_k} + a_{I,J} \phi_m^{I,J}, \tag{12}$$

where

$$a_{i_k} = \sqrt{\Gamma^k_{I,J}} \exp\left(\sqrt{\Gamma^k_{I,J}} x_k\right) + \frac{\sqrt{\Gamma^k_{I,J}} \lambda(x_k)}{\gamma(L_k)} \exp\left(\sqrt{\Gamma^k_{I,J}} L_k\right) \tag{13a}$$

$$a_{j_k} = - \frac{\sqrt{\Gamma^k_{I,J}} \lambda(x_k)}{\gamma(L_k)} \tag{13b}$$

$$a_{I,J} = - \sqrt{\Gamma^k_{I,J}} \exp\left(\sqrt{\Gamma^k_{I,J}} x_k\right) + \frac{\sqrt{\Gamma^k_{I,J}} \lambda(x_k)}{\gamma(L_k)} \left[1 - \exp\left(\sqrt{\Gamma^k_{I,J}} L_k\right)\right] \tag{13c}$$

with

$$\lambda(x_k) = \exp\left(\sqrt{\Gamma^k_{I,J}} x_k\right) + \exp\left(-\sqrt{\Gamma^k_{I,J}} x_k\right).$$

Combining expressions (10) and (12) for each node of the domain leads to a linear system where the unknowns are the values for the steady-state electric potential at the fracture segment nodes and in the matrix blocks. It is important to note that, at this stage, the number of equations in this system is less than the number of unknowns. Additional equations will complete the system through consideration of charge conservation in the matrix in Section 2.6. Note also that when the block-scale exchange coefficient $\alpha^{I,J}_{fm}$ tends to zero in the above equations, the coefficients a_{i_k}, a_{j_k}, and $a_{I,J}$ approach values of $-1/L_k$, $1/L_k$, and 0, respectively, leading to $\partial\phi^k_f/\partial x_k = 0$. This corresponds to the standard DFN approach.

2.6. Modified finite-volume approach for the matrix domain

To complete our model, we now consider equation (2) at the scale of the matrix blocks where, as in our analytical formulation for the distribution of electric potential along a fracture segment, the source term corresponds to electric current flow between the fractures and matrix and is designated by Q_{fm}. Integrating equation (2) over the matrix control volume $V_{I,J}$ and again making use of Gauss' Divergence Theorem, we arrive at

$$-\int_{S_{I,J}} (\sigma_m \nabla \phi_m) \cdot \vec{n}_{S_{I,J}} dS = \int_{V_{I,J}} Q_{fm} dV \tag{14}$$

where $S_{I,J}$ corresponds to the surface contour of $V_{I,J}$ and $\vec{n}_{S_i}$ is its outward unit normal vector. The left-hand side of equation (14) can be discretized using the finite-volume method as follows:

$$\begin{aligned}
&-\int_{S_{I,J}} (\sigma_m \nabla \phi_m) \cdot \vec{n}_{S_{I,J}} dS = \qquad (15)\\
&\sigma_m^E \left(\phi_m^{I,J} - \phi_m^{I-1,J}\right) - \sigma_m^W \left(\phi_m^{I+1,J} - \phi_m^{I,J}\right)\\
&+ \sigma_m^S \left(\phi_m^{I,J} - \phi_m^{I,J-1}\right) - \sigma_m^N \left(\phi_m^{I,J+1} - \phi_m^{I,J}\right).
\end{aligned}$$

The coefficients σ_m^E, σ_m^W, σ_m^S and σ_m^N correspond to the east, west, south and north directions, respectively, and are expressed as

$$\sigma_m^E = \frac{\Delta y}{\Delta x} \sigma_m^{[(I-1,J),(I,J)]} \tag{16a}$$

$$\sigma_m^W = \frac{\Delta y}{\Delta x} \sigma_m^{[(I,J),(I+1,J)]} \tag{16b}$$

$$\sigma_m^S = \frac{\Delta x}{\Delta y} \sigma_m^{[(I,J),(I,J-1)]} \tag{16c}$$

$$\sigma_m^N = \frac{\Delta x}{\Delta y} \sigma_m^{[(I,J),(I,J+1)]} \tag{16d}$$

where Δx and Δy are the longitudinal and transverse block lengths, respectively, and the terms $\sigma_m^{[(I,J),(K,L)]}$ represent the matrix conductivity between blocks (I, J) and (K, L) and are evaluated as the geometric average of the conductivities of these blocks.

Because current flow exchange only occurs along fracture segments located within the control volume $V_{I,J}$, Q_{fm} will be non-zero only along the fractures within that volume.

As a result, the right-hand side of equation (14) can be rewritten as

$$\int_{V_{I,J}} Q_{fm} dV = \sum_{k=1}^{N_f^{I,J}} \int_0^{L_k} Q_{fm} dx_k \tag{17}$$

where $N_f^{I,J}$ is the number of fracture segments contained in $V_{I,J}$. Combining expressions (17) and (4) leads to

$$\int_{V_{I,J}} Q_{fm} dV = -\alpha_{fm}^{I,J} \phi_m^{I,J} \sum_{k=1}^{N_{I,J}^f} L_k + \alpha_{fm}^{I,J} \sum_{k=1}^{N_{I,J}^f} \tilde{\phi}_f^k \tag{18}$$

where

$$\tilde{\phi}_f^k = \int_0^{L_k} \phi_f^k dx_k. \tag{19}$$

Using the analytical expression for the electric potential along a fracture segment given by equation (8), the integrated potential $\tilde{\phi}_f^k$ can then be expressed as

$$\tilde{\phi}_f^k = c_{i_k} \varphi_f^{i_k} + c_{j_k} \varphi_f^{j_k} + c_{I,J} \phi_{I,J}^m, \tag{20}$$

with

$$c_{i_k} = \int_0^{L_k} \beta(x_k) dx_k \tag{21a}$$

$$c_{j_k} = \int_0^{L_k} \frac{\gamma(x_k)}{\gamma(L_k)} dx_k \tag{21b}$$

$$c_{I,J} = \int_0^{L_k} \left[1 - \frac{\gamma(x_k)}{\gamma(L_k)} - \beta(x_k) \right] dx_k. \tag{21c}$$

This can also be expressed as

$$
\begin{aligned}
c_{i_k} =& \frac{\exp\left(\sqrt{\Gamma_{I,J}^k} L_k\right) - 1}{\sqrt{\Gamma_{I,J}^k}} & \text{(22a)}\\
&+ \frac{\exp\left(\sqrt{\Gamma_{I,J}^k} L_k\right)}{\sqrt{\Gamma_{I,J}^k} \gamma(L_k)}\\
&\times \left[\exp\left(-\sqrt{\Gamma_{I,J}^k} L_k\right) + \exp\left(\sqrt{\Gamma_{I,J}^k} L_k\right) - 2\right]\\
c_{j_k} =& - \frac{\exp\left(-\sqrt{\Gamma_{I,J}^k} L_k\right) + \exp\left(\sqrt{\Gamma_{I,J}^k} L_k\right) - 2}{\gamma(L_k)\sqrt{\Gamma_{I,J}^k}} & \text{(22b)}\\
c_{I,J} =& L_k - c_{j_k} - c_{i_k}. & \text{(22c)}
\end{aligned}
$$

This leads to the following expression of the fracture-matrix current flow exchange integrated over the control volume $V_{I,J}$

$$
\begin{aligned}
\int_{V_{I,J}} Q_{fm} dV = \phi_m^{I,J} \alpha_{fm}^{I,J} & \left[- \sum_{k=1}^{N_{I,J}^f} L_k + \sum_{k=1}^{N_{I,J}^f} c_{I,J} \right] & \text{(23)}\\
&+ \alpha_{fm}^{I,J} \sum_{k=1}^{N_{I,J}^f} \left[c_{i_k} \varphi_f^{i_k} + c_{j_k} \varphi_f^{j_k} \right].
\end{aligned}
$$

Combining expressions (15) and (23) in equation (14) leads to the following expression of charge conservation for the matrix block (I, J):

$$
\begin{aligned}
& A_{I,J}\phi_m^{I,J} + A_{I-1,J}\phi_m^{I-1,J} + A_{I+1,J}\phi_m^{I+1,J} & \text{(24)}\\
& + A_{I,J-1}\phi_m^{I,J-1} + A_{I,J+1}\phi_m^{I,J+1}\\
& - \alpha_{fm}^{I,J} \sum_{k=1}^{N_{I,J}^f} \left[c_{i_k} \varphi_f^{i_k} + c_{j_k} \varphi_f^{j_k} \right] = 0
\end{aligned}
$$

where

$$A_{I-1,J} = -\frac{\Delta y}{\Delta x}\sigma_m^{[(I-1,J),(I,J)]} \tag{25a}$$

$$A_{I+1,J} = -\frac{\Delta y}{\Delta x}\sigma_m^{[(I,J),(I+1,J)]} \tag{25b}$$

$$A_{I,J-1} = -\frac{\Delta x}{\Delta y}\sigma_m^{[(I,J),(I,J-1)]} \tag{25c}$$

$$A_{I,J+1} = -\frac{\Delta x}{\Delta y}\sigma_m^{[(I,J),(I,J+1)]} \tag{25d}$$

$$\begin{aligned} A_{I,J} = &-\left(A_{I-1,J} + A_{I+1,J} + A_{I,J-1} + A_{I,J+1}\right) \\ &+ \alpha_{fm}^{I,J}\left[\sum_{k=1}^{N_{I,J}^f} L_k - \sum_{k=1}^{N_{I,J}^f} c_{I,J}\right]. \end{aligned} \tag{25e}$$

Applying the above expression to each matrix block of the domain leads to a linear system where the unknowns are again the values for the steady-state electric potential at the fracture segment nodes and in the matrix blocks. This system, comprised of $N_X \cdot N_Y$ equations, completes the linear system derived in Section 2.5 for the fracture network. The final combined linear system expresses electric charge conservation in the fractures and in the matrix and accounts for current flow exchange between these two domains. It allows for determination of the electric potential at the fracture segment extremities as well as in the control volumes of the porous domain.

2.7. Fracture-matrix exchange coefficient

An important component of our numerical modeling approach, not discussed until now, is the choice of the block-scale exchange coefficient $\alpha_{fm}^{I,J}$, which controls the amount of electric current flow exchange between the fracture network and surrounding matrix. For *standard* dual porosity (DP) modeling of groundwater flow and solute transport in fractured media (i.e., where the fractures are not represented explicitly but rather as a secondary discretized domain with prescribed effective properties), many previous studies have been devoted to the evaluation of the exchange coefficient between the fracture and matrix domains. Investigations based on simplified geological scenarios have demonstrated that the coefficient is primarily dependent upon the properties and chosen discretization of the matrix. For example, considering normal sets of fractures and matrix blocks having simple regular shapes, basic expressions for the DP exchange coefficient can be deduced from simplified analytical solutions of the diffusion equation [*Haggerty and Gorelick*, 1995; *Warren and Root*, 1963]. In order to better represent the transient dynamics of flow exchange and/or more realistic geological scenarios, a wide variety of alternative formulations have also been proposed [*Carrera et al.*, 1998; *Dykhuizen*, 1990; *Haggerty and Gorelick*, 1995; *Haggerty et al.*, 2000; *Noetinger et al.*, 2001; *Zimmerman et al.*, 1993; *Alboin et al.*, 2002; *Kfoury et al.*, 2004; *Noetinger and Estebenet*, 2000; *Zyvoloski et al.*, 2008]. Note, however, that very few studies have considered evaluation of the fracture-matrix exchange coefficient for *discrete* dual porosity (DDP) modeling, where the fractures are represented explicitly rather than homogenized.

In the present work, we base our choice of the expression for $\alpha_{fm}^{I,J}$ on previous hydrological studies on fracture-matrix exchange at the fracture scale [*Roubinet et al.*, 2012] and on DDP modeling at the fracture-network scale [*Lee et al.*, 2001; *Li and Lee*, 2008]. *Roubinet et al.* [2012] demonstrated that, at the fracture scale, flow exchange is driven by the minimal diffusive transverse component of the system. *Li and Lee* [2008] justified that the pressure around a fracture is linearly distributed. These two observations lead us to the expression

$$\alpha_{fm}^{I,J} = \frac{min(\sigma_{I,J}^{m}, \sigma_{I,J}^{f})}{< d >}, \tag{26}$$

where $\sigma^m_{I,J}$ and $\sigma^f_{I,J}$ are the matrix and fracture electrical conductivities of the control volume $V_{I,J}$, with $\sigma^f_{I,J}$ defined as the average of the conductivities of the fractures contained within that volume. Here, $< d >$ represents the average normal distance between the fractures in the volume and the matrix block volume [*Li and Lee*, 2008]. As will be seen in the following section, the above formulation for $\alpha^{I,J}_{fm}$ appears to be a valid and accurate means of representing the fracture-matrix exchange for the electric current flow problem. Note, however, that our DDP formulation can be easily adapted to consider alternative expressions for $\alpha^{I,J}_{fm}$, and that this is a topic requiring further investigation.

3. Model validation

In order to validate our DDP modeling approach for electric current flow, we compare results obtained for the equivalent horizontal electrical conductivity of three different fracture networks with corresponding analytical and fully discretized numerical solutions. The considered fracture networks, shown in Figure 4, build in their complexity from left to right and are evaluated over a wide range of matrix-to-fracture electrical conductivity ratios that we believe to be representative of values potentially encountered in the field. Specifically, considering that the electrical conductivity of natural groundwater varies from 3×10^{-3} to 2×10^{-1} S m^{-1}, and that the conductivity of graphite and quartz are roughly 7×10^4 S m^{-1} and 5×10^{-15} S m^{-1}, respectively [*Schon*, 2011], we consider a range for σ_m/σ_f between 10^{-10} and 1 S m^{-1} for the validation. This is accomplished by holding fixed $\sigma_f = 10^{-2}$ S m^{-1} and varying σ_m from 10^{-12} to 10^{-2} S m^{-1}. In each case, a square domain of side length L is considered with Dirichlet boundary conditions for the electric potential equal to 1 V and 0 V on the left and right sides, respectively, and varying linearly between these values along the top and bottom sides. This results in electric current flow from left to right through the domain. The equivalent horizontal electrical conductivity σ_{eq} is then defined as the electric flux leaving the right side of the domain multiplied by the side length L.

3.1. Single set of parallel fractures

We first consider a domain of size $L = 10$ m consisting of 10 equally spaced horizontal fractures having constant aperture b_f (Figure 4a). For this simple configuration, the results for σ_{eq} obtained using our DDP approach can be validated against the following analytical solution:

$$\sigma_{eq} = \left[\sum_{i=1}^{N_f} b_f \sigma_f + \left(L - \sum_{i=1}^{N_f} b_f \right) \sigma_m \right] / L, \tag{27}$$

where $N_f = 10$ is the number of fractures. Three cases involving fracture apertures of 10^{-5}, 10^{-4}, and 10^{-3} m are considered.

Figure 5 shows the equivalent horizontal conductivity, obtained using our DDP model and using equation 27, as a function of the ratio σ_m/σ_f. A line indicating the electrical conductivity of the matrix is also presented for reference. Values for σ_{eq} can be seen to differ from the matrix conductivity when σ_m/σ_f falls below approximately 10^{-2}, indicating the point where the presence of fractures begins to impact the electrical conductivity of the domain. When σ_m/σ_f falls below approximately 10^{-6}, we see that there is essentially no further change in the equivalent conductivity, which corresponds to the case where the matrix conductivity is so low that current flow occurs only through the fractures, and thus where the use of a standard DFN approach would provide accurate solutions. The effect of the fracture aperture on the equivalent conductivity becomes clearly visible for small values of σ_m/σ_f, where σ_{eq} is seen to increase by one order of magnitude when the fracture aperture is increased by one order of magnitude. The excellent agreement between the equivalent conductivities evaluated using equation (27) and those obtained using our DDP approach confirms the ability of our model to deal with the domain presented in Figure 4a.

3.2. Two sets of orthogonal fractures

We next consider a domain of size $L = 1$ m consisting of 10 equally spaced horizontal fractures and 10 equally spaced vertical fractures having constant aperture $b_f = 10^{-3}$ m (Figure 4b). Here, we compare the results obtained for σ_{eq} using our DDP model with fully discretized finite-element solutions performed using the COMSOL Multiphysics software package. The number of fractures in this example required a reduction in the size of the domain from the previous example in order for the finite-element solutions to proceed in a reasonable time frame. Using the default meshing options in COMSOL, 332'046 triangular model elements were required to describe the 1×1 m region. In contrast, each DDP simulation was conducted using a 3×3 block discretization for the matrix, which led to a linear system containing only 189 unknowns. Figure 6 shows the validation results, where again we see an excellent agreement between the values for σ_{eq} obtained using our modeling approach and those obtained with COMSOL over the entire range of σ_m/σ_f ratios considered.

3.3. Random fracture network

For our final validation example, we consider a domain of size $L = 10$ m containing a random distribution of 9 fractures (Figure 4c), whose positions and angles were drawn from a uniform distribution and whose lengths are power-law distributed with exponent $a = 1.5$ and percolation parameter $p = 6$. A constant fracture aperture of $b_f = 10^{-3}$ m is assumed. Detailed descriptions of the power-law generation parameters and justifications concerning their ability to represent realistic fracture networks can be found in *Bonnet et al.* [2001], *Bour and Davy* [1997], and *Roubinet et al.* [2010a]. Again, results for σ_{eq} obtained using our DDP model are compared with fully discretized finite-element solutions computed using the COMSOL Multiphysics software package (Figure 7). In this case, using the default meshing options in COMSOL, 1'569'757 triangular model elements were required to describe the 10 $\times$ 10 m region, whereas our DDP code with a 10 $\times$ 10 block discretization for the matrix resulted in a linear system containing only 211 unknowns. We see yet again excellent agreement between our code and the finite-element solutions over the range of σ_m/σ_f values considered.

4. Examples

4.1. Electrical resistivity anisotropy of fractured media

As a first example showing the application of our DDP approach for modeling electric current flow in fractured rock, we consider the effect of fractures on the equivalent electrical resistivity ($\rho_{eq} = 1/\sigma_{eq}$) of several large-scale domains, specifically with regard to how ρ_{eq} changes as a function of the direction of the measurement. That is, we demonstrate how the modeling approach presented in Section 2 allows for efficient calculation of ρ_{eq} for large and potentially dense fracture networks, and we investigate how the presence of fractures impacts the overall anisotropic electrical properties. Knowledge regarding the effect of fractures on the electrical resistivity as a function of direction is critical to learning what information about fracture networks may be contained in geoelectrical data, as well as to understanding under what conditions an REV, and thus tensor representation, of the electrical resistivity may be safely assumed.

We consider below the anisotropic equivalent resistivity of several sets of regular fractures (Section 4.1.1), as well as of a series of hierarchical fracture networks (Section 4.1.2), all of which are defined over a square domain having side length $L = 100$ m with fixed matrix conductivity $\sigma_m = 10^{-4}$ S m^{-1}. To calculate ρ_{eq} as a function of direction in each case, we extract from the center of this domain a smaller square of side length $L = 50$ m at different orientations. As was done for the validation of our model, Dirichlet boundary conditions are assumed on the edges of this smaller square with the electric potential set to 1 V and 0 V on one set of opposing sides, and linearly varying between these two values on the other set of opposing sides. The equivalent resistivity is then calculated based on the electric flux leaving the zero-potential side of the domain. To visualize and characterize the anisotropic electrical properties, we follow the methodology described in *Long et al.* [1982] for studying permeability anisotropy in fractured media, where a polar plot of the inverse square root of the equivalent permeability is created. For isotropic materials, the polar plot results in a circle. For anisotropic materials with two main directions of anisotropy, the polar plot will be an ellipse. In complex and realistic fractured media, a non-symmetric shape often results because tensorial properties cannot be assumed at the scale of the measurement [*Long et al.*, 1982; *Roubinet et al.*, 2010a]. For each example presented below, we similarly examine polar plots where the radius is the square root of the equivalent resistivity ($\sqrt{\rho_{eq}}$), which is the electrical counterpart to the inverse square root of the equivalent permeability in hydrological studies.

4.1.1. Sets of regular fractures

Figure 8 shows the three sets of regular fractures that were considered for the anisotropic analysis. Fracture set FS1 (Figure 8a) is defined by 40 horizontal fractures having aperture

$b_f = 10^{-3}$ m and electrical conductivity $\sigma_f = 10^{-1}$ S m^{-1}. Fracture sets FS2 (Figure 8b) and FS3 (Figure 8c) were created through the superposition upon this first set of fractures a second group of 10 fractures oriented at an angle of 50 degrees and having aperture $b_f = 10^{-2}$ m and conductivity $\sigma_f = 10^{-1}$ S m^{-1}. In FS2, the second group of fractures has a homogeneous spatial distribution, whereas in FS3 a centered distribution with a fracture spacing of 1 m was considered. Please note that only the central extractions from the three studied domains, corresponding to a rotation angle of zero degrees, are shown in Figure 8.

Figure 9 shows the resulting polar plots of the square root of the equivalent electrical resistivity corresponding to FS1, FS2, and FS3. Also shown is the curve corresponding to the case of no fractures, where only the matrix is represented. In general, we see that the presence of fractures noticeably decreases the equivalent resistivity when the fractures connect the sides of the domain across which the potential gradient was applied and the resistivity measurement was made. Indeed, for fracture set FS1, we observe that ρ_{eq} is noticeably smaller than for the case of no fractures, except at orientation angles near 90 and 270 degrees where such a connection does not occur. Also notice for FS1 how, in going from the case of no fractures to a set of uniformly distributed fractures, the equivalent resistivity turns from isotropic to anisotropic with a well defined elliptical behavior. For the case of fracture sets FS2 and FS3, we observe an even stronger anisotropic behavior as a result of the addition of the second group of fractures. Again, ρ_{eq} decreases most along orientations where the fractures best connect the domain. Note, however, the strong effect of the particular fracture configuration on the nature of the resistivity anisotropy, as seen by comparing the polar plots for FS2 and FS3. For the FS3 case, the equivalent resistivity cannot be well described by an ellipse and thus a tensor representation at this scale would be inappropriate.

4.1.2. Hierarchical fracture networks

We next evaluate the anisotropic behavior of the equivalent electrical resistivity for a series of hierarchical fracture networks (Figure 10). To this end, we consider Sierpinski lattices, which are simple geometrical structures thought to be representative of the fractal properties observed in natural fracture networks (e.g., *Doughty and Karasaki* [2002]; *Roubinet et al.* [2013, 2010b]). The lattices are generated by successively dividing and replicating an initial pattern at different scales. They are characterized by their level of division k, where $k = 1$, 2, 3 and 4 for the example structures S1, S2, S3, and S4 in Figure 10, respectively. For all of the structures shown, we consider a constant fracture aperture and electrical conductivity of $b_f = 10^{-3}$ m and $\sigma_f = 10^{-2}$ S m^{-1}, respectively.

Figure 11 shows the polar plots of the square root of the equivalent resistivity corresponding to fracture networks S1, S2, S3, and S4, along with the curve for the case of no fractures. Given that the polar plot for network S1 is isotropic and nearly identical to that for the no-fractures case, it is clear that this configuration does not contain enough fractures to noticeably impact the overall resistivity of the domain. After increasing the level of division of the Sierpinski structures to $k \geq 2$, we see a local increase in ρ_{eq} for angles between 30 and 150 degrees. This results because, at these orientation angles, the presence of small fractures has the effect of connecting the 'upstream' side of the domain (where the electric potential was set to 1 V) to its adjacent sides, but not to the opposite 'downstream' side (where the potential was set to 0 V), thus reducing the flow of electric current in the direction of the measurement. Adding fractures to the network amplifies this phenomenon, as seen by the increase in this local perturbation when going from network S2 to network S3. However, the similar results obtained for configurations S3 and S4 show that, beyond a given level of division (here $k = 3$), the fractures added by increasing k are too small to impact the equivalent domain properties. These results suggest that the impact of fractures on ρ_{eq} critically depends on the localization and properties of those fractures. Previously, for the regular sets of fractures considered in Figures 8 and 9, additional fractures crossing the entire domain were found to decrease the equivalent resistivity. Here we see the opposite effect, in the sense that adding small fractures deviates the main electric flow. This effect, however, is observed only down to a certain 'minimal length' of the added fractures. It suggests that the detection of fractures by electrical survey methods may be restricted to a specific range of fracture lengths, and that modeling tools such as the presented DDP approach could be of particular interest to determine this specific range.

4.2. Electric potential distribution for a point-current-injection source

As a second and final example showing the application and flexibility of our modeling methodology, we evaluate the steady-state spatial distribution of electric potential corresponding to a point-current-injection source. This is done for a series of large-scale fracture networks that vary in terms of their fracture density and statistical characteristics. Our reason for choosing this particular example is that modeling the spatial distribution of electric potential for a point source forms a critical component of the numerical simulation of geoelectrical survey data. In other words, the following application represents an important first step towards being able to explore what information may be contained in such data concerning fracture, and fracture network, characteristics.

We consider as before a square domain having side length $L = 100$ m, but now with an electric-current point-source term of density 1 A m^{-2} located in the middle of the upper boundary of this domain. That is, we consider the injection of a 1-A current into the domain at this location. To represent what would be encountered along the surface of the Earth, the top of the domain is prescribed a no-flow (Neumann) boundary condition, which is expressed as

$$\frac{\partial \phi}{\partial \vec{n}} = 0, \tag{28}$$

where ϕ is the electric potential and $\vec{n}$ is the outward normal vector to the boundary. For the other three boundaries, we consider mixed conditions defined by

$$\frac{\partial \phi}{\partial \vec{n}} + \beta \phi = 0, \tag{29}$$

where $\beta = \vec{n} \cdot \frac{\vec{r}}{|r^2|}$ and $\vec{r}$ is the vector from the source term to the considered position. Such mixed boundaries are commonly used in the modeling of geoelectrical survey data, as they allow for the natural propagation of electric current without requiring enlargement of the simulation domain (e.g., *Blome et al.* [2009]; *Dey and Morrison* [1979]; *Li and Spitzer* [2002]).

Figure 12 shows the different fracture networks that were considered for this example. In all cases, the fracture aperture was set to $b_f = 10^{-3}$ m and the electrical conductivity to $\sigma_f = 10^{-1}$ S m^{-1}. A conductivity value of $\sigma_m = 10^{-3}$ S m^{-1} was assumed for the matrix. To create these different networks, fracture positions and angles were drawn from uniform distributions, whereas fracture lengths were assumed to be power-law distributed with exponent a and percolation parameter p. The latter parameter allows control over the fracture density [*Bonnet et al.*, 2001; *Bour and Davy*, 1997; *Roubinet et al.*, 2010a].

Figure 13 shows the calculated spatial distribution of the electric potential corresponding to the different fracture configurations in Figure 12. In Figure 13a, we see the result for the case of no fractures, which is simply the electric potential distribution corresponding to a point-electric-current injection into a homogeneous half-space. As fractures are added to the matrix (Figure 13b-h), notice how the potential distribution changes markedly because the fractures allow significantly greater electrical connection between different parts of the domain. In general, this distribution is highly non-uniform, suggesting that the use of any kind of large-scale equivalent properties in such domains would be inappropriate. An exception is when a highly dense fracture network is considered such as that shown in Figure 12h. Here, we see that the corresponding potential distribution approaches the form of that seen for the homogeneous half-space in Figure 12a, albeit with lower overall values because of the increase in overall conductivity provided by the fractures. That is, when the fracture density becomes great enough to connect equally well all parts of the domain, the domain can again be viewed as an effective homogeneous medium.

5. Discussion and conclusions

We have presented in this paper a discrete-dual-porosity approach for the numerical modeling of electric current flow in fractured rock. The foundation of our method is an analytical formulation for fracture-matrix flow exchange at the fracture scale, which is integrated into modified DFN and modified finite-volume numerical solutions for the fracture network and matrix, respectively. This leads to an innovative approach where current flow can be accurately evaluated in complex fractured media over large spatial scales at extremely low computational cost. Indeed, the size of the linear system solved using our DDP methodology was found to be orders-of-magnitude smaller than the number of triangular elements required by commercial finite-element software for the two validation examples considered in Sections 3.2 and 3.3. Although admittedly the computational cost of such fully discretized solutions is highly dependent on the particular details of the meshing technique and/or type of discretization used [*Bing and Greenhalgh*, 2001; *Pichot et al.*, 2010], it is quite evident that the approach presented here will offer significant computational benefits against even the most efficient implementations.

In order to find an optimal balance between computational cost and representation accuracy, our modeling approach relies on a number of assumptions, both at the fracture and fracture-network scales. Two of the key assumptions made in this work are (i) that fractures can be accurately represented by lower-dimensional geometrical elements (e.g., lines instead of two-dimensional structures); and (ii) that fracture-matrix current flow exchange can be accurately represented as the product of a block-scale exchange coefficient and the difference in electric potential between the fractures and matrix. As seen in our model validations, the latter assumption appears to be completely valid for the large-scale simulations considered in this paper. However, both assumptions should be carefully considered before widespread use of the presented approach for different purposes and/or under different conditions and scales. In particular, future work will investigate the sensitivity of our proposed methodology to different formulations for the fracture-matrix exchange coefficient. An additional limitation with our modeling approach may be met in the case of a fracture isolated inside a matrix block. So far, the electric current flow in such a fracture is not considered in our model because there will be no potential difference between the two fracture extremities. This problem may be avoided by reducing the block size of the porous domain until the isolated fracture is contained in at least two matrix blocks. Another solution could be to integrate the effect of the isolated fracture into the matrix block conductivity, as has been done in previous DDP work in hydrology [*Lee et al.*, 2001].

Finally, it is important to emphasize that only a 2D modeling approach has been presented in this paper. Clearly, for the numerical simulation of real-world geoelectrical survey data using point electrodes, a fully 3D formulation, or at the very least a 2.5D implementation, are required. Nonetheless, the work presented here represents a critical first step towards these goals, and should be eventually extendable to three dimensions with suitable modification and development, albeit at the expense of significantly greater model complexity. In addition, the 2D modeling methodology presented in this paper allows exploration of a number of interesting and important questions with regard to the use of geoelectrical measurements in fractured-rock environments. These include at what scale there will exist an REV for the electrical resistivity for different types of fracture networks, as well as how different network characteristics affect the bulk geoelectrical response. Despite an abundant field evidence demonstrating the effect of fractures on geoelectrical data and potential links to hydraulically relevant properties, these types of questions could not be explored previously in the context of realistic and large-scale fracture networks because of a lack of suitable numerical modeling tools.

References

Alboin, C., J. Jaffre, P. Joly, J. Roberts, and C. Serres (2002), A comparison of methods for calculating the matrix block source term in a double porosity model for contaminant transport, *Computational Geosciences*, *6*(3-4), 523–543, doi:10.1023/A:1021259702179.

Berg, S., and E. Oian (2007), Hierarchical approach for simulating fluid flow in normal fault zones, *Petroleum Geoscience*, *13*(1), 25–35, doi:10.1144/1354-079305-676.

Berkowitz, B. (2002), Characterizing flow and transport in fractured geological media: A review, *Advances in Water Resources*, *25*(8-12), 861–884, doi:10.1016/S0309-1708(02)00042-8.

Berryman, J. G., and G. M. Hoversten (2013), Modelling electrical conductivity for earth media with macroscopic fluid-filled fractures, *Geophysical Prospecting*, *61*(2), 471–493, doi:10.1111/j.1365-2478.2012.01135.x.

Bing, Z., and S. Greenhalgh (2001), Finite element three-dimensional direct current resistivity modelling: accuracy and efficiency considerations, *Geophysical Journal International*, *145*(3), 679–688, doi:10.1046/j.0956-540x.2001.01412.x.

Blome, M., H. R. Maurer, and K. Schmidt (2009), Advances in three-dimensional geoelectric forward solver techniques, *Geophysical Journal International*, *176*(3), 740–752, doi:10.1111/j.1365-246X.2008.04006.x.

Boadu, F. K., J. Gyamfi, and E. Owusu (2005), Determining subsurface fracture characteristics from azimuthal resistivity surveys: A case study at nsawam, ghana, *Geophysics*, *70*(5), B35–B42, doi:10.1190/1.2073888.

Bonnet, E., O. Bour, N. Odling, P. Davy, I. Main, P. Cowie, and B. Berkowitz (2001), Scaling of fracture systems in geological media, *Reviews of Geophysics*, *39*(3), 347–383, doi:10.1029/1999RG000074.

Bour, O., and P. Davy (1997), Connectivity of random fault networks following a power law fault length distribution, *Water Resour. Res.*, *33*(7), 1567–1583, doi:10.1029/96WR00433.

Busby, J. P. (2000), The effectiveness of azimuthal apparent-resistivity measurements as a method for determining fracture strike orientations, *Geophysical Prospecting*, *48*(4), 677–695, doi:10.1046/j.1365-2478.2000.00208.x.

Cacas, M., E. Ledoux, G. de Marsily, B. Tillie, A. Barbreau, E. Durand, B. Feuga, and P. Peaudecerf (1990), Modeling fracture flow with a stochastic discrete fracture network; calibration and validation; 1, the flow model, *Water Resources Research*, *26*(3), 479–489, doi:10.1029/WR026i003p00479.

Campbell, D. L. (1977), Model for estimating electric macro-anisotropy coefficient of aquifers with horizontal and vertical fractures, *Geophysics*, *42*(1), 114–117, doi:10.1190/1.1440705.

Carneiro, J. (2009), Numerical simulations on the influence of matrix diffusion to carbon sequestration in double porosity fissured aquifers, *International Journal of Greenhouse Gas Control*, *3*(4), 431–443, doi:10.1016/j.ijggc.2009.02.006.

Carrera, J., X. Sanchez-Vila, I. Benet, A. Medina, G. Galarza, and J. Guimera (1998), On matrix diffusion: formulations, solution methods and qualitative effects, *Hydrogeology Journal*, *6*(1), 178–190, doi:10.1007/s100400050143.

Crank, J. (1975), *The mathematics of diffusion*, 2d ed.oxford: ed., Clarendon Press.

Cvetkovic, V., S. Painter, N. Outters, and J. Selroos (2004), Stochastic simulation of radionuclide migration in discretely fractured rock near the aspo hard rock laboratory, *Water Resources Research*, *40*(2), W02404, doi:10.1029/2003wr002655.

Davy, P., O. Bour, J. R. D. Dreuzy, and C. Darcel (2006), Flow in multiscale fractal fracture networks, *Geological Society, London, Special Publications*, *261*(1), 31–45, doi:10.1144/GSL.SP.2006.261.01.03.

Day-Lewis, F. (2003), Time-lapse imaging of saline-tracer transport in fractured rock using difference-attenuation radar tomography, *Water Resources Research*, *39*(10), doi:10.1029/2002WR001722.

de Dreuzy, J.-R., G. Pichot, B. Poirriez, and J. Erhel (2013), Synthetic benchmark for modeling flow in 3d fractured media, *Computers and Geosciences*, *50*, 59–71, doi:10.1016/j.cageo.2012.07.025.

Dershowitz, W., and H. Einstein (1988), Characterizing rock joint geometry with joint system models, *Rock Mechanics and Rock Engineering*, *21*(1), 21–51, doi:10.1007/BF01019674.

Dershowitz, W., and C. Fidelibus (1999), Derivation of equivalent pipe networks analogues for three-dimensional discrete fracture networks by the boundary element method, *Water Resources Research*, *35*(9), 2685–2691, doi:10.1029/1999WR900118.

Dershowitz, W., and I. Miller (1995), Dual-porosity fracture flow and transport, *Geophysical Research Letters*, *22*(11), 1441–1444, doi:10.1029/95GL01099.

Dey, A., and H. Morrison (1979), Resistivity modeling for arbitrarily shaped three-dimensional structures, *Geophysics*, *44*(4), 753–780, doi:10.1190/1.1440975.

Donadille, J.-M., and S. Al-Ofi (2012), Crosswell electromagnetic response in a fractured medium, *Geophysics*, *77*(3), D53–D61, doi:10.1190/geo2011-0227.1.

Dorn, C., N. Linde, T. L. Borgne, O. Bour, and L. Baron (2011), Single-hole gpr reflection imaging of solute transport in a granitic aquifer, *Geophysical Research Letters*, *38*(8), doi:10.1029/2011GL047152.

Dorn, C., N. Linde, J. Doetsch, T. L. Borgne, and O. Bour (2012), Fracture imaging within a granitic rock aquifer using multiple-offset single-hole and cross-hole gpr reflection data, *Journal of Applied Geophysics*, *78*, 123–132, doi:10.1016/j.jappgeo.2011.01.010.

Doughty, C., and K. Karasaki (2002), Flow and transport in hierarchically fractured rock, *Journal of Hydrology*, *263*(1-4), 1–22, doi:10.1016/S0022-1694(02)00032-X.

Dverstop, B., and J. Andersson (1989), Application of the discrete fracture network concept with field data: possibilities of model calibration and validation, *Water Resources Research*, *25*(3), 540–550, doi:10.1029/WR025i003p00540.

Dykhuizen, R. (1990), A new coupling term for dual-porosity models, *Water Resources Research*, *26*(2), 351–356, doi:10.1029/WR026i002p00351.

Gautam, P., and K. Mohanty (2004), Matrix-fracture transfer through countercurrent imbibition in presence of fracture fluid flow, *Transp. Porous Media*, *55*(3), 309–337, doi:10.1023/B:TIPM.0000013326.95597.10.

Haegland, H., A. Assteerawatt, H. K. Dahle, G. Eigestad, and R. Helmig (2009), Comparison of cell- and vertex-centered discretization methods for flow in a two-dimensional discrete-fracture-matrix system, *Advances in Water Resources*, *32*(12), 1740–1755, doi:10.1016/j.advwatres.2009.09.006.

Haggerty, R., and S. M. Gorelick (1995), Multiple-rate mass-transfer for modeling diffusion and surface-reactions in media with pore-scale heterogeneity, *Water Resources Research*, *31*(10), 2383–2400, doi:10.1029/95WR10583.

Haggerty, R., S. A. McKenna, and L. C. Meigs (2000), On the late-time behavior of tracer test breakthrough curves, *Water Resources Research*, *36*(12), 3467–3479, pT: J; TC: 128; UT: WOS:000165799100006.

Herwanger, J., M. Worthington, R. Lubbe, A. Binley, and J. Khazanehdari (2004a), A comparison of cross-hole electrical and seismic data in fractured rock, *Geophysical*

Prospecting, *52*(1), 109–121, doi:10.1046/j.1365-2478.2003.00402.x.

Herwanger, J., C. Pain, A. Binley, C. de Oliveira, and M. Worthington (2004b), Anisotropic resistivity tomography, *Geophysical Journal International*, *158*(2), 409–425, doi:10.1111/j.1365-246X.2004.02314.x.

Jinsong, S., S. Benyu, and G. Naichuan (2009), Anisotropic characteristics of electrical responses of fractured reservoir with multiple sets of fractures, *Petroleum Science*, *6*(2), 127–138, doi:10.1007/s12182-009-0021-0.

Kfoury, M., R. Ababou, B. Noetinger, and M. Quintard (2004), Matrix-fracture exchange in a fractured porous medium: stochastic upscaling, *Compte Rendus Mecanique*, *332*(8), 679–686, doi:10.1016/j.crme.2004.04.001.

Kolditz, O., and C. Clauser (1998), Numerical simulation of flow and heat transfer in fractured crystalline rocks: Application to the hot dry rock site in rosemanowes (uk), *Geothermics*, *27*(1), 1–23, doi:10.1016/S0375-6505(97)00021-7.

Krautblatter, M., S. Verleysdonk, A. Flores-Orozco, and A. Kemna (2010), Temperature-calibrated imaging of seasonal changes in permafrost rock walls by quantitative electrical resistivity tomography, *Journal of Geophysical Research*, *115*(F02003), doi:10.1029/2008JF001209.

Lane, J., F. Haeni, and W. Watson (1995), Use of square-array direct-current resistivity method to detect fractures in crystalline bedrock in new hampshire, *Ground Water*, *33*(3), 476–485, doi:10.1111/j.1745-6584.1995.tb00304.x.

Lee, S., L. M.F., and J. C.L. (2001), Hierarchical modeling of flow in naturally fractured formations with multiple length scales, *Water Resour. Res.*, *37*(3), 443–456, doi:10.1029/2000WR900340.

Li, L., and S. Lee (2008), Efficient field-scale simulation of black oil in a naturally fractured reservoir through discrete fracture networks and homogenized media, *SPE Res Eval and Eng*, *11*(4), 750–758.

Li, Y., and K. Spitzer (2002), Three-dimensional dc resistivity forward modelling using finite elements in comparison with finite-difference solutions, *Geophysical Journal International*, *151*(3), 924–934, doi:10.1046/j.1365-246X.2002.01819.x.

Liu, E. (2005), Effects of fracture aperture and roughness on hydraulic and mechanical properties of rocks: implication of seismic characterization of fractured reservoirs, *Journal of Geophysics and Engineering*, *2*(1), 38–47, doi:10.1088/1742-2132/2/1/006.

Lofi, J., P. Pezard, D. Loggia, E. Garel, S. Gautier, C. Merry, and K. Bondabou (2012), Geological discontinuities, main flow path and chemical alteration in a marly hill prone to slope instability: Assessment from petrophysical measurements and borehole image analysis, *Hydrological Processes*, *26*(14), 2071–2084, doi:10.1002/hyp.7997.

Long, J. C. S., J. S. Remer, C. R. Wilson, and P. A. Witherspoon (1982), Porous-media equivalents for networks of discontinuous fractures, *Water Resources Research*, *18*(3), doi:10.1029/WR018i003p00645.

Lubbe, R., and M. Worthington (2006), A field investigation of fracture compliance, *Geophysical Prospecting*, *54*(3), 319–331, doi:10.1111/j.1365-2478.2006.00530.x.

Majer, E., J. Peterson, T. Daley, B. Kaelin, L. Myer, J. Queen, P. DOnfro, and W. Rizer (1997), Fracture detection using crosswell and single well surveys, *Geophysics*, *62*(2), 495–504, doi:10.1190/1.1444160.

Neuman, S. P. (2005), Trends, prospects and challenges in quantifying flow and transport through fractured rocks, *Hydrogeology Journal*, *13*(1), 124–147, doi:10.1007/s10040-004-

0397-2.

Noetinger, B., and T. Estebenet (2000), Up-scaling of double porosity fractured media using continuous-time random walks methods, *Transport in Porous Media*, *39*(3), 315–337, doi:10.1023/A:1006639025910.

Noetinger, B., T. Estebenet, and P. Landereau (2001), A direct determination of the transient exchange term of fractured media using a continuous time random walk method, *Transport in Porous Media*, *44*(3), doi:10.1023/A:1010647108341.

Pehme, P., B. Parker, J. Cherry, J. Molson, and J. Greenhouse (2013), Enhanced detection of hydraulically active fractures by temperature profiling in lined heated bedrock boreholes, *Journal of Hydrology*, *484*, 1–15, doi:10.1016/j.jhydrol.2012.12.048.

Pichot, G., J. Erhel, and J. R. de Dreuzy (2010), A mixed hybrid mortar method for solving flow in discrete fracture networks, *Applicable Analysis*, *89*(10), 1629–1643, doi:10.1080/00036811.2010.495333.

Pichot, G., J. Erhel, and J.-R. de Dreuzy (2012), A generalized mixed hybrid mortar method for solving flow in stochastic discrete fracture networks, *SIAM Journal on scientific computing*, *34*(1), B86–B105, doi:10.1137/100804383.

Pidlisecky, A., and R. Knight (2008), Fw2_5d: A matlab 2.5-d electrical resistivity modeling code, *Computers and Geosciences*, *34*(12), 1645–1654, doi:10.1016/j.cageo.2008.04.001.

Pytharouli, S., R. Lunn, Z. Shipton, J. Kirkpatrick, and A. do Nascimento (2011), Microseismicity illuminates open fractures in the shallow crust, *Geophysical Research Letters*, *38*(2), doi:10.1029/2010GL045875.

Queen, J., and W. Rizer (1990), An integrated study of seismic anisotropy and the natural fracture system at the conoco borehole test facility, kay county, oklahoma, *Journal of Geophysical Research-Solid Earth and Planets*, *95*(B7), 11,255–11,273, doi:10.1029/JB095iB07p11255.

Robinson, J., T. Johnson, and L. Slater (2013), Evaluation of known-boundary and resistivity constraints for improving cross-borehole dc electrical resistivity imaging of discrete fractures, *Geophysics*, *78*(3), D115–D127, doi:10.1190/geo2012-0333.1.

Rotter, B., D. Barry, J. Gerhard, and J. Small (2008), Modeling u(vi) biomineralization in single- and dual-porosity porous media, *Water Resour. Res.*, *44*(8), doi:10.1029/2007wr006301.

Roubinet, D., J.-R. de Dreuzy, and P. Davy (2010a), Connectivity-consistent mapping method for 2-d discrete fracture networks, *Water Resources Research*, *46*, W07532, doi:10.1029/2009WR008302.

Roubinet, D., H.-H. Liu, and J.-R. de Dreuzy (2010b), A new particle-tracking approach to simulating transport in heterogeneous fractured porous media, *Water Resources Research*, *46*, W11507, doi:10.1029/2010WR009371.

Roubinet, D., J. R. de Dreuzy, and D. M. Tartakovsky (2012), Semi-analytical solutions for solute transport and exchange in fractured porous media, *Water Resources Research*, *48*, W01542, doi:10.1029/2011WR01116.

Roubinet, D., J.-R. de Dreuzy, and D. M. Tartakovsky (2013), Particle-tracking simulations of anomalous transport in hierarchically fractured rocks, *Computers and Geosciences*, *50*(0), 52–58, doi:10.1016/j.cageo.2012.07.032.

Rücker, C., T. Günther, and K. Spitzer (2006), Three-dimensional modelling and inversion of dc resistivity data incorporating topography ? i. modelling, *Geophys. J. Int.*, *166*(2), 495–505, doi:10.1111/j.1365-246X.2006.03010.x.

Schmutz, M., A. Ghorbani, P. Vaudelet, and A. Revil (2011), Spectral induced polarization detects cracks and distinguishes between open- and clay-filled fractures, *Journal of Environmental and Engineering Geophysics*, *16*(2), 85–91, doi:10.1190/geo2011-0227.1.

Schon, J. (2011), Physical properties of rocks - a workbook, *Elsevier*, *8*(1st Edition), 494.

Talley, J., G. Baker, M. Becker, and N. Beyrle (2005), Four dimensional mapping of tracer channelization in subhorizontal bedrock fractures using surface ground penetrating radar, *Geophysical Research Letters*, *32*(4), doi:10.1029/2004GL021974.

Taylor, R., and A. Fleming (1988), Characterizing jointed systems by azimuthal resistivity surveys, *Ground Water*, *26*(4), 464–474, doi:10.1111/j.1745-6584.1988.tb00413.x.

Tsoflias, G., and A. Hoch (2006), Investigating multi-polarization gpr wave transmission through thin layers: Implications for vertical fracture characterization, *Geophysical Research Letters*, *33*(20), doi:10.1029/2006GL027788.

Warren, J. E., and P. J. Root (1963), The behavior of naturally fractured reservoirs, *Society of Petroleum Engineers Journal*, *3*(3), 245–255.

Wishart, D., L. Slater, and A. Gates (2008), Fracture anisotropy characterization in crystalline bedrock using field scale azimuthal self potential gradient, *Journal of Hydrology*, *358*(1-2), 35–45, doi:10.1016/j.jhydrol.2008.05.017.

Zimmerman, R., G. Chen, T. Hadgu, and G. Bodvarsson (1993), A numerical dual-porosity model with semianalytical treatment of fracture matrix flow, *Water Resources Research*, *29*(7), 2127–2137, doi:10.1029/93WR00749.

Zyvoloski, G., B. Robinson, and H. Viswanathan (2008), Generalized dual porosity: A numerical method for representing spatially variable sub-grid scale processes, *Advances in Water Resources*, *31*(3), 535–544, doi:10.1016/j.advwatres.2007.11.006.

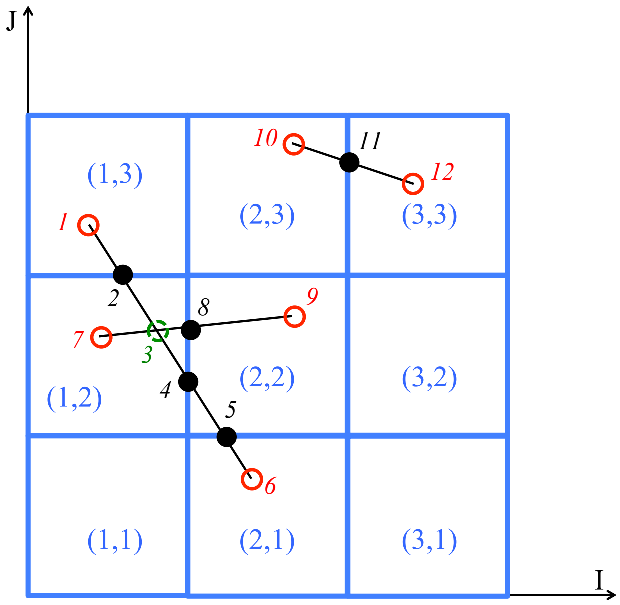

Figure 1. Discretization of the proposed discrete-dual-porosity model. The matrix is divided into regular blocks (blue squares) identified by indices (I, J), whereas the fractures are represented by 1D elements that have been subdivided into segments (black lines) whose endpoints are the nodes of the domain (numbered circles). The nodes consist of fracture extremities (red), fracture intersections (green), and intersections between fractures and matrix-block boundaries (black).

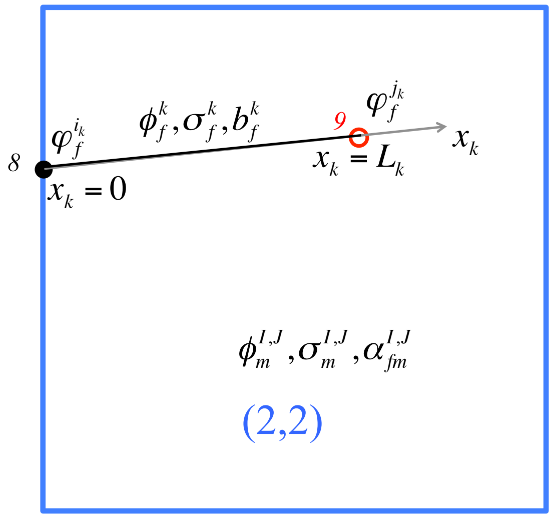

Figure 2. Zoom of matrix block $(2, 2)$ from Figure 1 showing only the fracture segment joining nodes 8 and 9. The endpoints of this k^{th} segment are located at $x_k = 0$ and $x_k = L_k$, where L_k is the length of the segment and x_k denotes the 1D spatial variable along the segment. The electrical conductivity of the segment is denoted by σ_f^k, the fracture aperture by b_f^k, and the electric potential by $\phi_f^k = \phi_f^k(x_k)$. Variables $\varphi_f^{i_k}$ and $\varphi_f^{j_k}$ refer to the electric potential at $x_k = 0$ and $x_k = L_k$, respectively. At the block scale, $\sigma_m^{I,J}$, $\phi_m^{I,J}$, and $\alpha_{fm}^{I,J}$ are used to denote the matrix electrical conductivity, matrix electric potential, and fracture-matrix exchange coefficient, respectively.

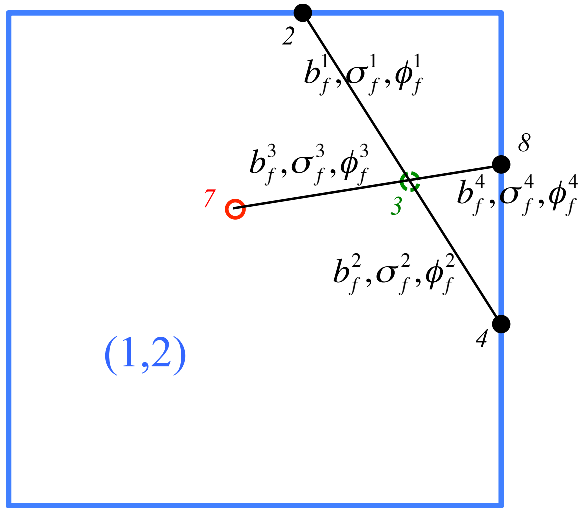

Figure 3. Zoom of matrix block $(1, 2)$ from Figure 1 showing the fracture intersection located at node 3. This node is the shared extremity of the fracture segments numbered $k = 1, 2, 3$, and 4, having nodes 2, 4, 7, and 8 as their second extremity, respectively. Each segment is characterized by its electrical conductivity σ_f^k, aperture b_f^k, and electric potential $\phi_f^k = \phi_f^k(x_k)$.

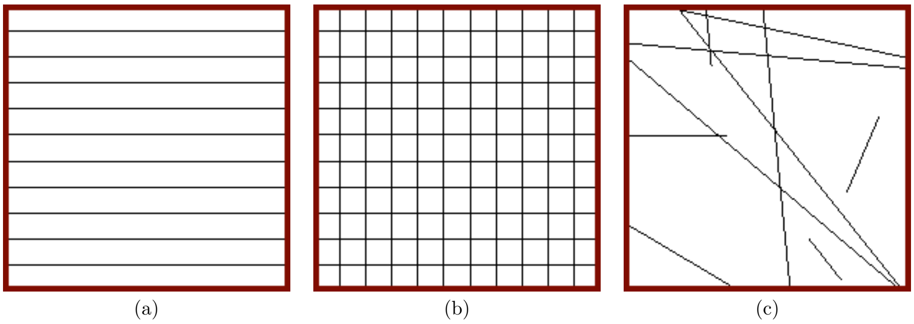

Figure 4. Fracture configurations used to validate our discrete-dual-porosity modeling approach. In each case a square domain of side length L is considered, and the equivalent resistivity in the horizontal direction is evaluated for matrix conductivities σ_m ranging from 10^{-10} to 1 S m^{-1}. The fracture conductivity is $\sigma_f = 10^{-2}$ S m^{-1}. (a) Set of 10 horizontal fractures with $L = 10$ m, and considering fracture apertures of $b_f = 10^{-5}$, 10^{-4}, and 10^{-3} m. (b) Set of 10 horizontal and 10 vertical fractures with $L = 1$ m and $b_f = 10^{-3}$ m. (c) Set of 9 randomly distributed fractures with $L = 10$ m and $b_f = 10^{-3}$ m.

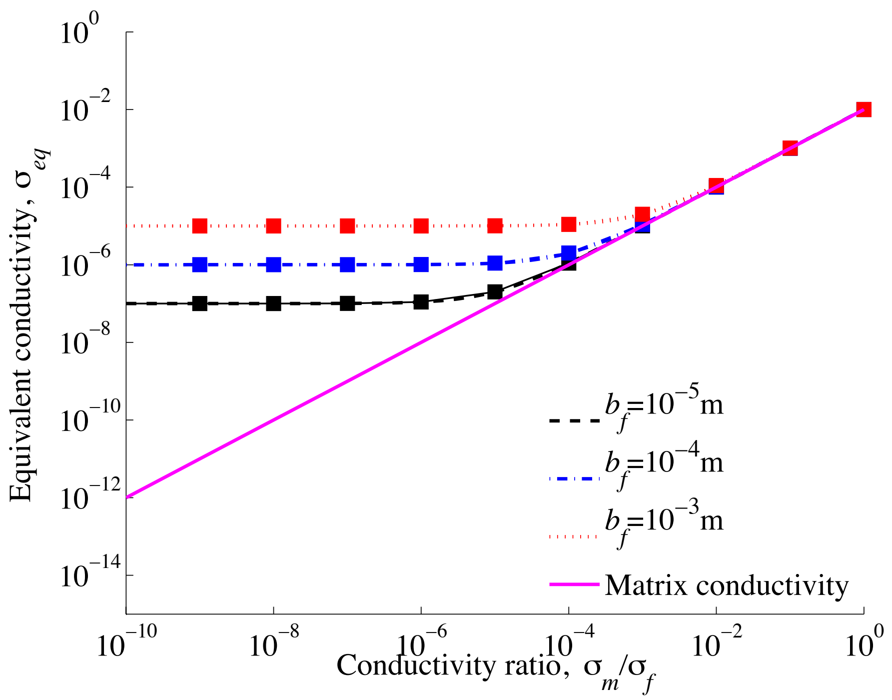

Figure 5. Equivalent electrical conductivity (in S m^{-1}) for the set of parallel fractures in Figure 4a, plotted as a function of matrix-to-fracture conductivity ratio and for different apertures. Results obtained using our discrete-dual-porosity model (dashed lines) are compared with the corresponding analytical solution (square markers). A solid line indicating the matrix conductivity is also shown for reference.

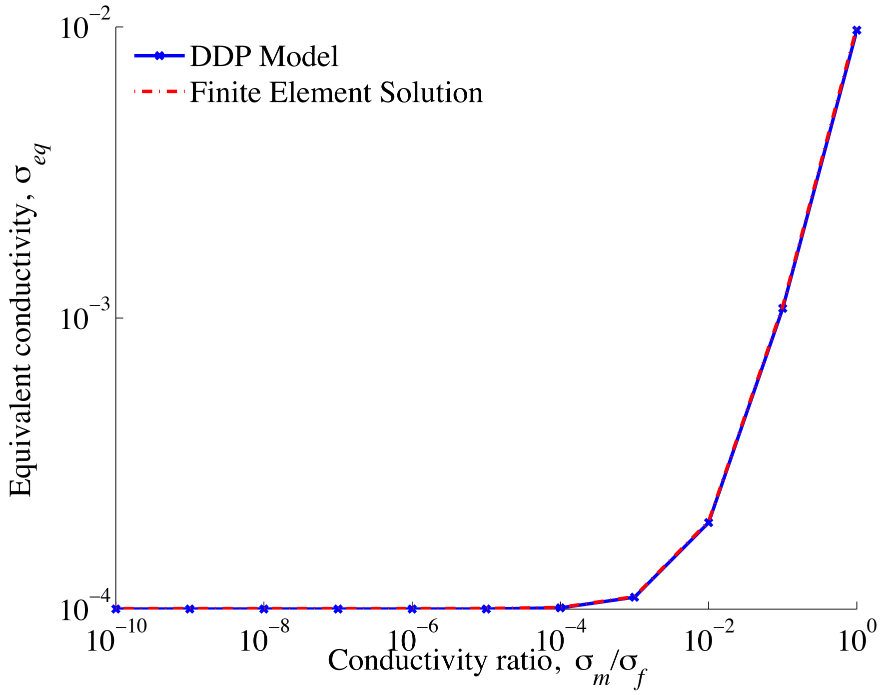

Figure 6. Equivalent electrical conductivity (in S m^{-1}) for the set of orthogonal fractures in Figure 4b, plotted as a function of matrix-to-fracture conductivity ratio. Results obtained using our discrete-dual-porosity model (blue) are compared with the results of fully discretized finite-element simulations performed using COMSOL (red).

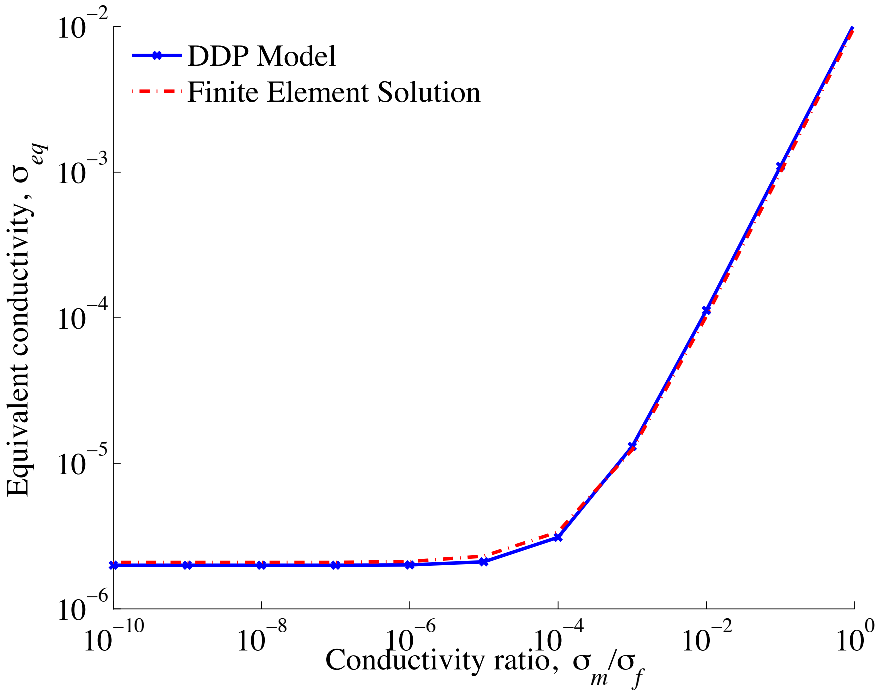

Figure 7. Equivalent electrical conductivity (in S m^{-1}) for the random fracture network in Figure 4c, plotted as a function of matrix-to-fracture conductivity ratio. Results obtained using our discrete-dual-porosity model (blue) are compared with the results of fully discretized finite-element simulations performed using COMSOL (red).

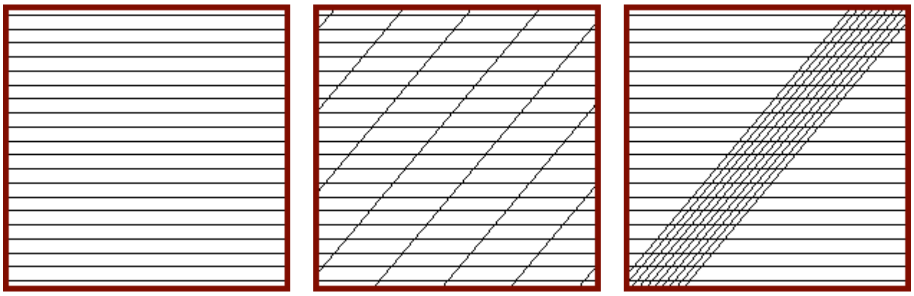

(a) FS1 (b) FS2 (c) FS3

Figure 8. Sets of regular fractures used to study the directional dependence of the equivalent electrical resistivity. The initial domain size is a square of side length $L = 100$ m, from which central squares of $L = 50$ m were extracted at different orientations. The matrix conductivity in all cases is $\sigma_m = 10^{-4}$ S m^{-1}. (a) Horizontal fractures having conductivity $\sigma_f = 10^{-1}$ S m^{-1} and aperture $b_f = 10^{-3}$ m. (b and c) Superposition of regular fractures oriented at an angle of 50 degrees to those in (a) and characterized by $\sigma_f = 10^{-1}$ S m^{-1} and $b_f = 10^{-2}$ m. The spatial distribution of the superimposed fractures is either (b) homogeneous or (c) centered and defined by a spacing of 1 m.

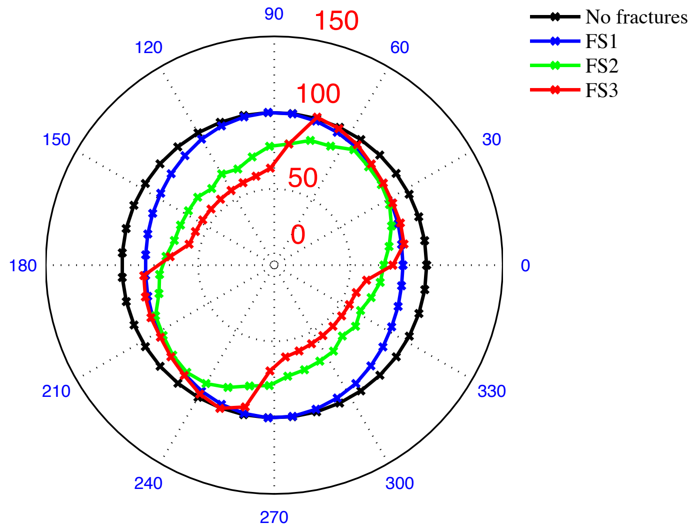

Figure 9. Polar plot of the square root of the equivalent electrical resistivity ρ_{eq}, in [Ohm m]$^{1/2}$ and represented by large red numbers, for the case of no fractures (black), and fracture sets FS1 (blue), FS2 (green), and FS3 (red) from Figure 8.

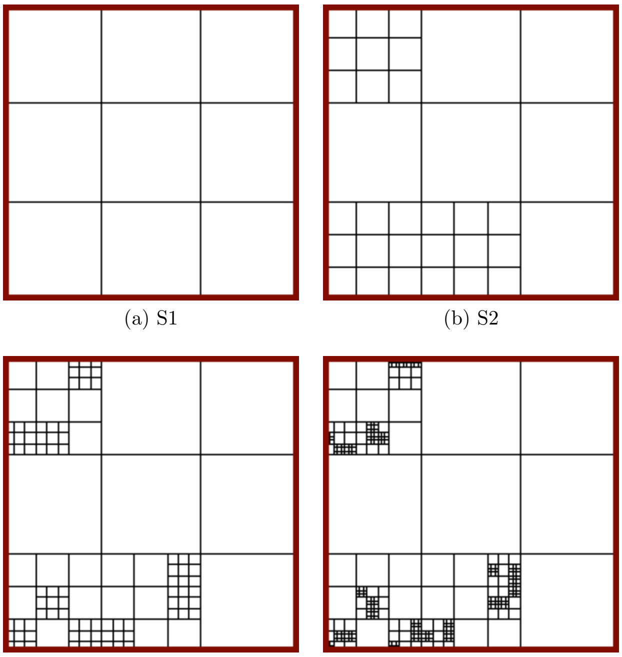

(a) S1 (b) S2 (c) S3 (d) S4

Figure 10. Sierpinski lattices used to study the directional dependence of the equivalent electrical resistivity. The initial domain size is a square of side length $L = 100$ m, from which central squares of $L = 50$ m were extracted at different orientations. The matrix and fracture conductivities in all cases are $\sigma_m = 10^{-4}$ S m^{-1} and $\sigma_f = 10^{-2}$ S m^{-1}. The fracture aperture is $b_f = 10^{-3}$ m. The different lattices were generated with (a) one, (b) two, (c) three, and (d) four levels of division.

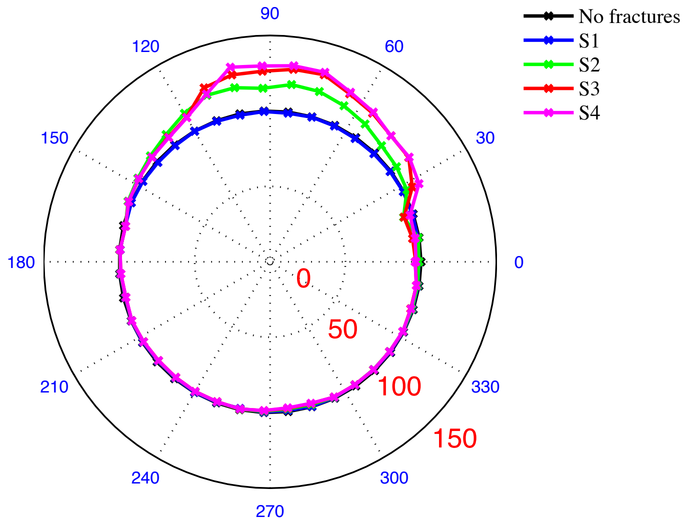

Figure 11. Polar plot of the square root of the equivalent electrical resistivity ρ_{eq}, in [Ohm m]$^{1/2}$ and represented by large red numbers, for the case of no fractures (black), and fracture sets S1 (blue), S2 (green), S3 (red), and S4 (purple) from Figure 10.

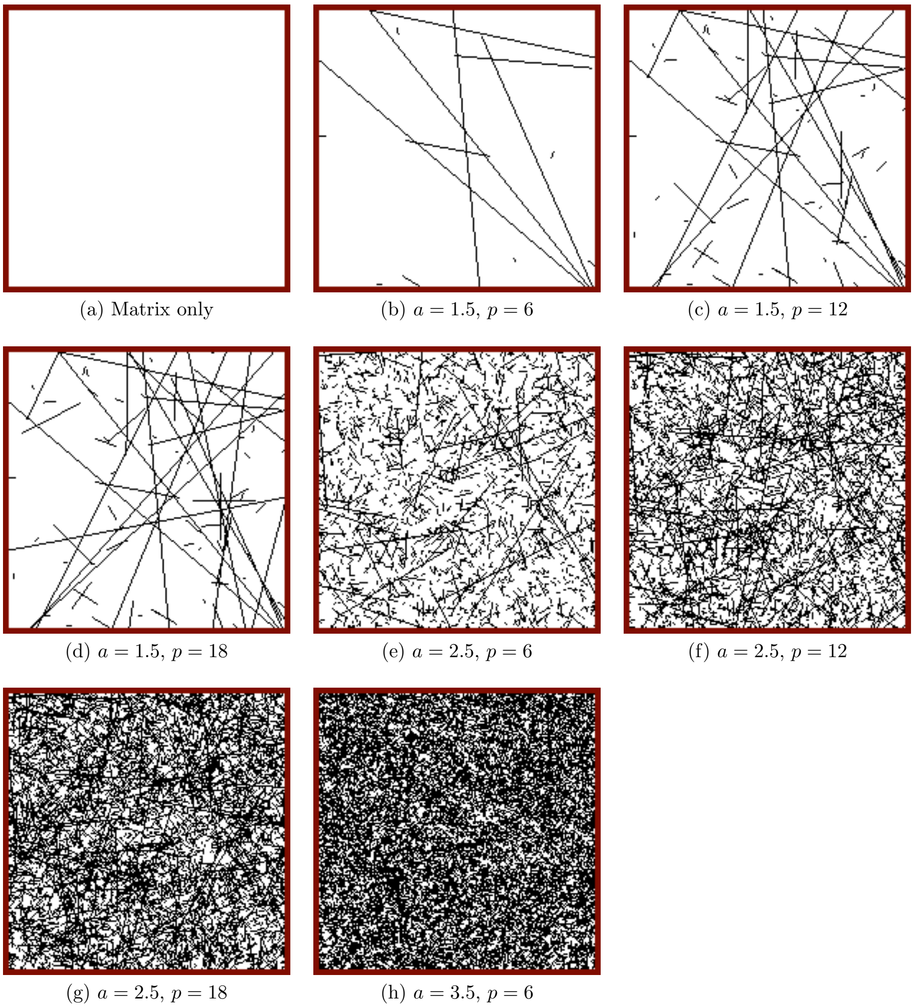

Figure 12. Random fracture networks upon which we investigate the effect of a point-electric-current source on the spatial distribution of the electric potential. The fractures are defined in a square domain having side length $L = 100$ m. Fracture positions and angles are uniformly distributed, whereas fracture lengths are power-law distributed with exponent a and percolation parameter p. The fractures are embedded in a matrix of conductivity $\sigma_m = 10^{-3}$ S m^{-1}. All fractures have aperture $b_f = 10^{-3}$ m and conductivity $\sigma_f = 10^{-1}$ S m^{-1}.

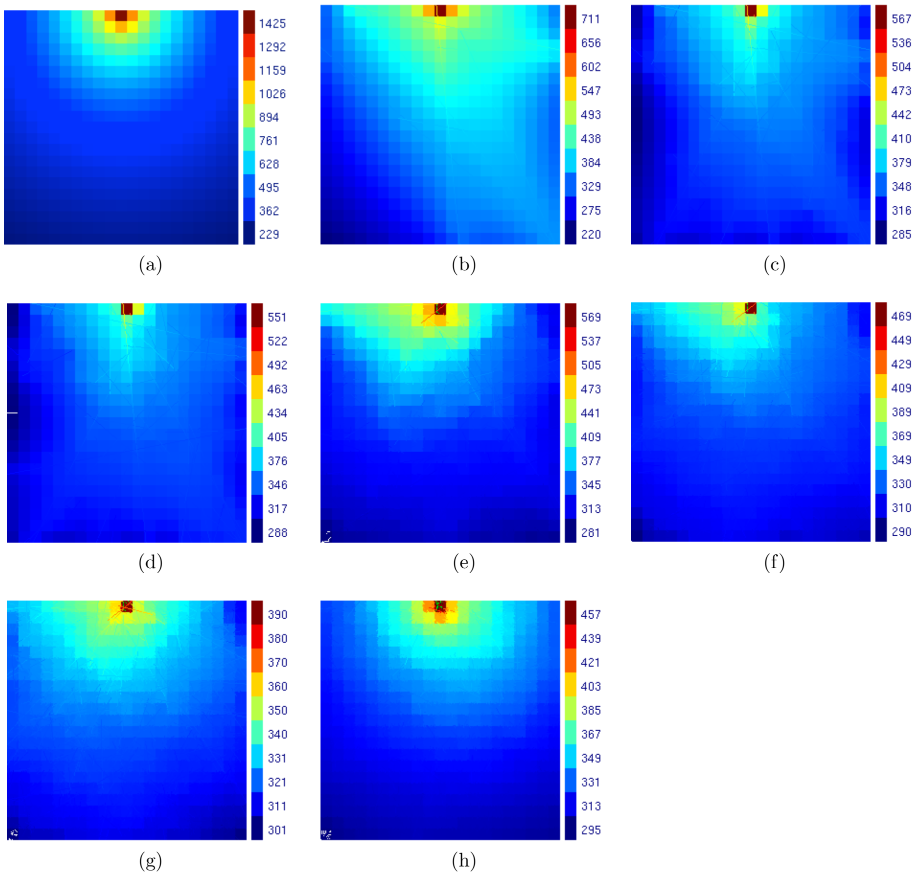

Figure 13. Spatial distribution of the electric potential (in Volts) corresponding to the fracture networks shown in Figure 12, resulting from a point-electric-current injection of 1 A in the middle of the upper boundary of the domain.